Supplementary Information for

Coulombically-stabilized oxygen hole polarons enable fully reversible oxygen redox

Iwnetim I. Abate[1,2], C. Das Pemmaraju[2], Se Young Kim[3], Kuan H. Hsu[1], Sami Sainio[4], Brian Moritz[2], John Vinson[5], Michael F. Toney[1,4], Wanli Yang[6], William E. Gent[1], Thomas P. Devereaux[1,2*], Linda F. Nazar[3*], William C. Chueh[1,2,7*]

[1]Department of Materials Science and Engineering, Stanford University, 496 Lomita Mall, Stanford, CA 94305, USA.
[2]Stanford Institute for Materials & Energy Sciences, SLAC National Accelerator Laboratory, 2575 Sand Hill Road, Menlo Park, CA 94025, USA.
[3]Department of Chemistry and the Waterloo Institute for Nanotechnology, University of Waterloo, 200 University Avenue West, Waterloo, Ontario N2L 3G1, Canada.
[4]Stanford Synchrotron Radiation Light source, SLAC National Accelerator Laboratory, 2575 Sand Hill Road, Menlo Park, CA 94025, USA.
[5]Material Measurement Laboratory, National Institute of Standards and Technology, Gaithersburg, Maryland 20899, USA.
[6]Advanced Light Source, Lawrence Berkeley National Laboratory, Berkeley, CA 94720, USA.

*email: tpd@stanford.edu (T.P.D.), lfnazar@uwaterloo.ca (L.F.N.), wchueh@stanford.edu (W.C.C.)

This PDF file includes:

Materials and Methods
Supplementary Text
Figs. S1 to S14
Tables S1
References (SR1-24)

SUPPLEMENTAL EXPERIMENTAL PROCEDURES

Material synthesis

$Na_2Mn_3O_7$ powder was prepared by a solid-state method. A stoichiometric mixture of $NaNO_3$ (J. T. Baker, A.C.S. Reagent) and $MnCO_3$ (Aldrich, $\geq$ 99.9%) powder was ball-milled at 250 rpm for 1 h. The collected mixture powder was then heated at 600 °C (5 °C/min) for 12 h under an oxygen flow and naturally cooled down to room temperature (RT). The as prepared powder sample transferred directly to an argon filled glovebox (MBraun, O_2 and $H_2O \leq 0.1$ ppm) without exposure to the air.

Electrochemistry

Positive electrodes were prepared inside an argon filled glovebox (O_2 and H_2O < 1 ppm) to avoid air contamination. $Na_2Mn_3O_7$ powder was mixed with 10 wt% Super P carbon and 10 wt% polyvinylidene fluoride (PVDF) (Aldrich average Mw $\approx$ 534 000) and suspended in N-methyl-2-pyrrolidinone (Sigma-Aldrich, 99.5%). The slurry was cast on aluminum foil with an active material loading of 5 - 7 mg·cm^{-2}. The electrodes were punched to a 1 cm^2 geometric area and dried in a vacuum oven at 120 °C overnight. The electrochemical studies were carried out in 2325 coin-type half cells with Na metal-disk (Sigma-Aldrich, ACS reagent) as the counter electrode. The electrolyte was comprised of 1M $NaPF_6$ (Alfa Aesar, $\geq$ 99.0%) dissolved in a mixture of ethylene carbonate (BASF, 99.98%), propylene carbonate (BASF, 99.98%) and 4-fluoro-1,3-dioxolan-2-one (Sigma-Aldrich, 99%) with a volume ratio of 49:49:2. Glass fiber (Merck Millipore) was employed as a separator. Galvanostatic cycling was performed using a multi-channel battery tester (Model 4000, Maccor Inc.) at room temperature with a current density of C/20 (theoretical (de)intercalation of 2 Na^+ per $Na_2Mn_3O_7$ in 20 h).

XRD

High-resolution powder XRD patterns for Rietveld refinement were measured at beamline 2-1 at the Stanford Synchrotron Radiation Lightsource (SSRL, SLAC National Accelerator Laboratory) at 17 keV (0.7293 Å) beam energy. The size of the X-ray beam was 500 × 1500 μm^2 and the distance between sample and the Pilatus-100K detector was 700 mm. All of the samples were contained in capillaries to avoid possible preferred orientation of the particles. All of the samples were measured using transmission and $\theta - 2\theta$ geometry.

RIXS

O-K edge RIXS measurements were performed at the ultra-high efficiency iRIXS endstation at Beamline 8.0.1 of the Advanced Light Source (ALS) at the Lawrence Berkeley National Laboratory.[1] The electrodes were disassembled in a high-purity Ar environment after charging and transferred into the experimental vacuum chamber using a gas-tight sample-transfer vessel. The samples were then mounted at 45° to the incident X-ray beam, and the outgoing photon direction was 90° with respect to the incident beam. The excitation energy was calibrated at the beginning of the experiment using X-ray absorption spectroscopy (XAS) measurement of a single-crystal Ti_2O_5 reference sample to determine the energy shift. RIXS measurements were performed

every 0.2 eV. The emission energy was calibrated using the elastic line on the RIXS map. The samples were checked for radiation damage by looking for changes in the XAS spectrum before and after the RIXS measurement, and the damage was observed to be negligible.

Soft XAS

Mn-L edge and complimentary O-K edge XAS measurements were carried out at the Stanford Synchrotron Radiation Lightsource (SSRL) on a bending magnet beamline 8-2 using a 55° incidence angle (magic angle) of X-rays. Beamline 8-2 is equipped with a spherical grating monochromator which is operated using 40 x 40 μm slits. This results in a resolution of around 200 meV. The beam spot size at the interaction point was around 1 x 1 mm^2 with total flux on the order of 10^{10} photons / sec. The X-ray energy for the oxygen $1s$ edge were from 520 eV to 560 eV. The data was collected both in total electron yield (TEY) mode using the drain current amplified by a Keithley picoampmeter. The incoming flux was recorded using a nickel grid with Au sputtered film.

Hard XAS

XAS measurements in the hard X-ray regime were performed in transmission mode on intact electrodes harvested from charging and sealed under Ar in a polymer pouch. The measurement was performed at beamline 2-2 at the Stanford Synchrotron Radiation Laboratory using a Si (220) double crystal monochromator detuned to 50%–60% of its original intensity to eliminate high-order harmonics. The photon energy was calibrated using reference Mn foil by setting the first crossing of the second derivative of the absorbance spectrum to be 6539 eV. Three ion chambers (I_0, I_{sample}, and I_{ref}) were used simultaneously. The Athena software package was used to normalize and align the spectra.[2]

First-principles Simulations

Density Functional Theory (DFT) based ground state total energy simulations and structural optimizations were performed using the planewave platform VASP[3] within the projector augmented wave (PAW) potential framework.[4] A planewave energy cutoff of 500 eV was employed in conjunction with PAW potentials with valence electronic configurations of Na: [Ne] $3s^1$, Mn: [Ar] $4s^1$, $3d^6$ and O: [He] $2s^2$, $2p^4$. A 4×4×4 Γ-centered k-point mesh was used for Brillouin zone integration. Exchange-correlation (XC) effects were treated at the HSE06[5] screened hybrid functional level.

Structural optimization was performed on the experimentally determined structure for $Na_{2-x}Mn_3O_7$ which includes two formula units in the unit cell.[6] The stable magnetic configuration was identified as featuring high spin Mn^{4+} and in-plane ferromagnetic ordering between neighboring Mn sites. This configuration was used for structural studies. To prepare the 50% desodiated system, one Na atom per formula unit was removed from the simulation cell and the system geometry was re-optimized. We created the 1NN, 2NN, and 3NN configurations by slightly distorting the specific oxygen atoms to force localization on those oxygen atoms. We note that in SCF calculations coupled to DFT structural optimization, the system relaxes to the nearest local minimum. Each of the configurations we explored is a metastable minimum.

The relative chemical shift of the O-$1s$ core level associated with O$^-$ hole polaron sites in the desodiated structure was also estimated within a supercell approach using VASP. Accordingly, a 2×2×2 supercell of $Na_{2-x}Mn_3O_7$ with 192 atoms was set up and one Na atom was removed. Due to the large size of the supercell, this part of the simulation was carried out using the DFT+U [7] method with the PBE[8] semi-local XC functional and on-site Hubbard-U parameters U_d = 3.9 eV[9] U_{2p} = 6.0 eV[10] on Mn $3d$, O $2p$ orbitals respectively which are in the range adapted by earlier literature studies of transition metal oxides. Following structural optimization of an O$^-$ hole polaron configuration, the core-level eigenenergies of all the oxygen sites in the supercell were compared as shown in Fig. S8(B). The O$^-$ hole polaron site features a O-$1s$ core level that is roughly ~2 eV deeper in eigenenergy than that of the O^{2-} sites in the rest of the supercell. This *eigenenergy difference* provides an approximation to the relative chemical shift. Note that in Fig. S8(B), the core-level eigenenergies were rigidly shifted by 27 eV to facilitate comparison with photoemission data as absolute core binding energies are systematically underestimated by PBE eigenvalues.

Simulations of the XAS spectra were carried out using the OCEAN package[11,12] which implements the Bethe Salpeter Equation(BSE) formalism for core and valence excitations. Ground state single-particle orbital energies and wavefunctions needed by OCEAN were calculated using the QUANTUM ESPRESSO code[13] based on the lattice structures obtained above. For this purpose, norm-conserving pseudopotentials treating the Na:$3s$, O:$2s$, $2p$ and Mn:$3d$,$4s$ states in the valence were employed in conjunction with a planewave cutoff of 100 Ry. Brillouin zone integration was carried out employing Γ-centered 4x4x4 K-point grids.

Within OCEAN, the occupied and virtual single-particle energies and wavefunctions either from a Kohn-Sham (KS) DFT calculation or a quasiparticle theory like the GW method are used to solve the BSE in a two particle electron-hole basis.[14,15] In lieu of GW quasiparticle corrections, we employ a simple re-calibration of the DFT+U parameters and an additional scissor shift Δ_{CB} of the empty conduction band states so that the KS band gap and single-particle density of states (DOS) approximate that obtained from accurate Heyd-Scuseria-Ernzerhof (HSE)[16] screened hybrid functional studies. Accordingly we employ U_d = 1.5 eV, U_{2p} = 3.0 eV and Δ_{CB} =1.99 eV. The corresponding KS eigenvalues and eigenfunctions form inputs to OCEAN BSE. Within OCEAN the screened core-hole potential was calculated employing 392 bands over a 2 × 2 × 2 k-point grid. To obtain XAS spectra over an extended energy range, 160 bands were included in the BSE calculation. An O K-edge core-hole lifetime parameter of 0.4 eV was used in the simulations. Only dipole-allowed transitions were considered. The photon polarization vectors were set at [100], [010], and [001], and the final spectrum of each structure was obtained by averaging the spectra generated from using each of the polarization vectors. Since OCEAN is based on a pseudopotential method, an ad hoc rigid shift was applied to calibrate the incoming photon energy axis to facilitate comparison with experiment.
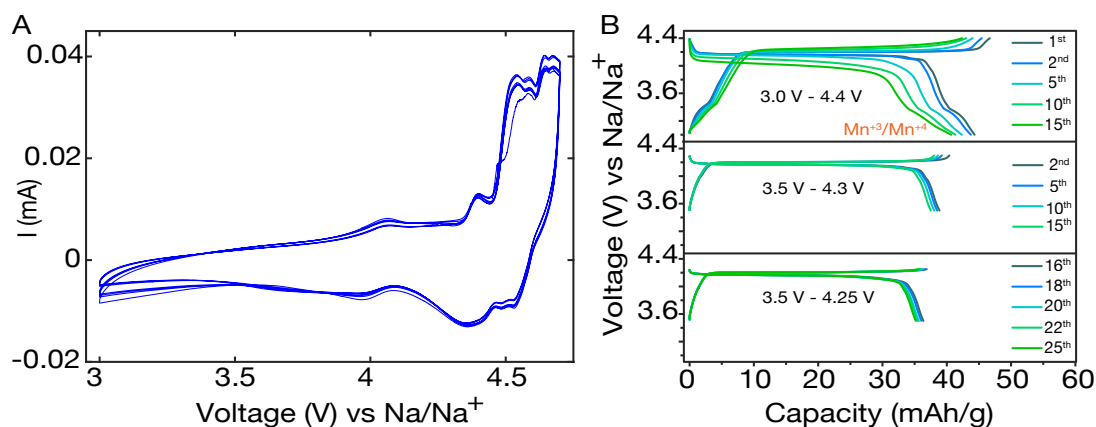
Supplementary Figures

Fig. S1. Determination of the optimum voltage window for cycling. (A) Cyclic voltammetry study in a coin cell (Na metal as anode, 1M NaClO$_4$ in PC as electrolyte and stainless steel as the counter electrode), showing that the electrolyte significantly degraded above 4.3 V due to side reactions. These reactions are avoided by using 4.3 V as the upper limit; (B) Investigation of reversibility with different voltage cut-off limits. As Mn$^{+3/+4}$ contributes to the capacity below 4.2 V (details are discussed in Fig. S5), an increase in the lower cut off from 3 V to 3.5 V enhances performance.
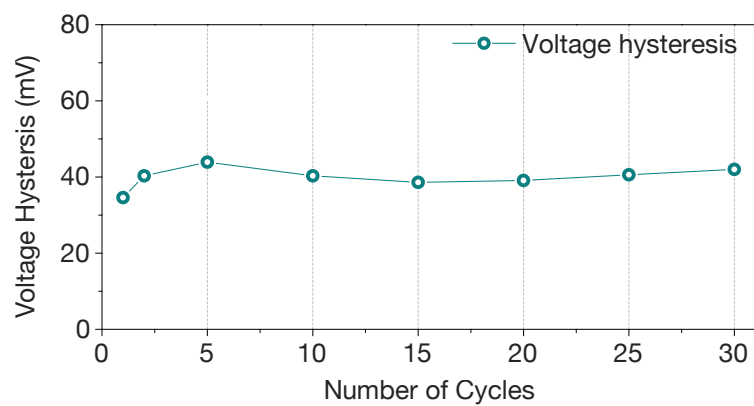
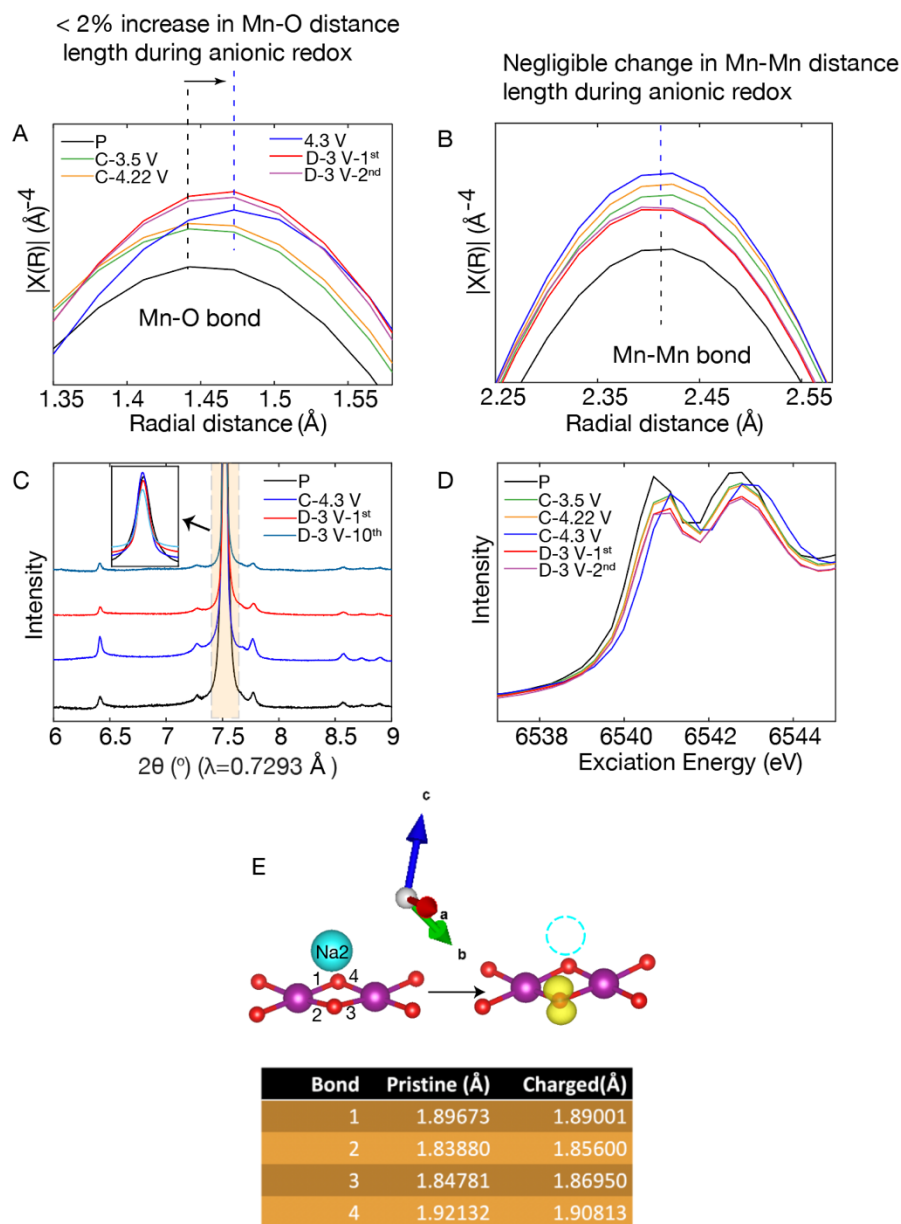**Fig. S2. Invariant low voltage hysteresis of ~40 mV between charge and discharge over cycling.**

Fig. S3. Structural stability during anionic redox. Examining changes in Mn-O distance (A) and Mn-Mn distance (B) upon charging. Zoomed in Fourier transform of the ex-situ EXAFS the pristine material (P) and electrodes charged to 3.5 V, 4.22 V, and 4.3 V in the 1st cycle and discharged to 3 V in the 1st and 2nd cycle (D-3V-1st and D-3V-10th), respectively. The negligible change in the EXAFS profile indicates local stability upon cycling. The bond length of Mn-O increases by only < 2% upon charging to 4.3 V while negligible changes in Mn-Mn bond length is observed. (C) Synchrotron powder X-ray diffraction at low angle (pristine, charged to 4.3 V and discharged to 3 V at 1st and 10th cycle). XRD patterns exhibit negligible changes indicating no structural modification. Inset shows the FWHM has negligible changes upon cycling. (D) Pre-edge from Mn-K edge XANES. The pre-edge has negligible changes which indicate local structural

stability and lack of Mn migration to tetrahedral site. (E) DFT also confirms the < 2% Mn-O bond length change upon charging. Upon the removal of sodium atoms during charging, the Mn-O bond length near the oxidized oxygen increases slightly (< 2%). The yellow dumbbells show the localized hole polaron on the oxidized oxygen which are discussed in detail in Fig. 3. These results are consistent with the above observations in EXAFS, XRD and XANES.
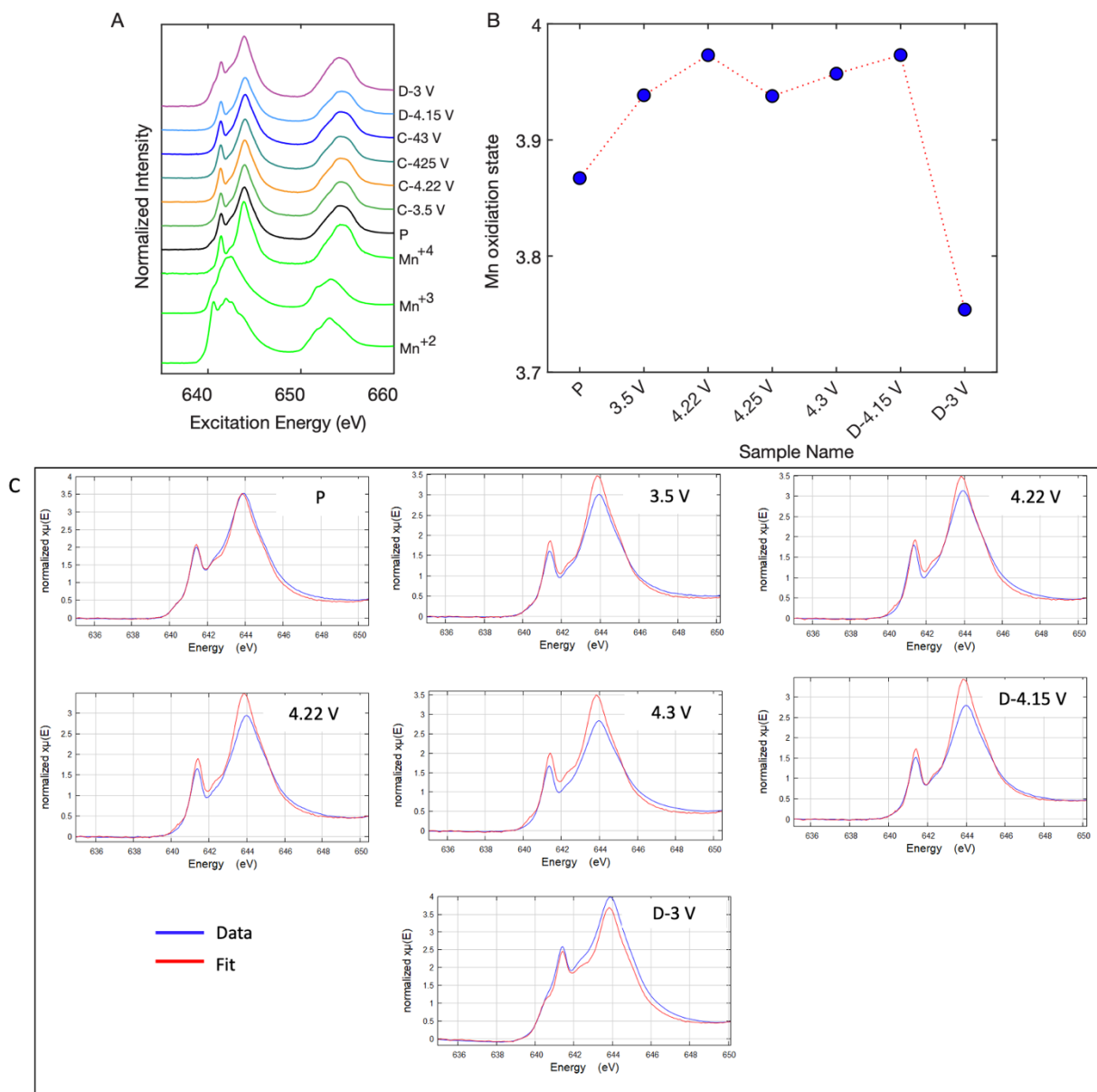

Fig. S4. Surface oxidation of Mn < 4.2 V. (A) Mn-L edge TEY-XAS. The green spectra are for reference compounds with Mn^{+2} (MnO), Mn^{+3} (Mn_3O_4) and Mn^{+4} ($Li_{1.17}Ni_{0.21}Co_{0.08}Mn_{0.54}O_2$). By linear combination fitting we estimated the Mn oxidation state in pristine $Na_2Mn_3O_7$ and changes upon charging (B). Mn changes the most from pristine to ~4.2V upon charging. Error bars for fitted bulk Mn states are smaller than the symbols and are therefore not shown. (C) Fits (red) of the Mn TEY-XAS (blue) with linear combinations of the reference spectra shown in (A).
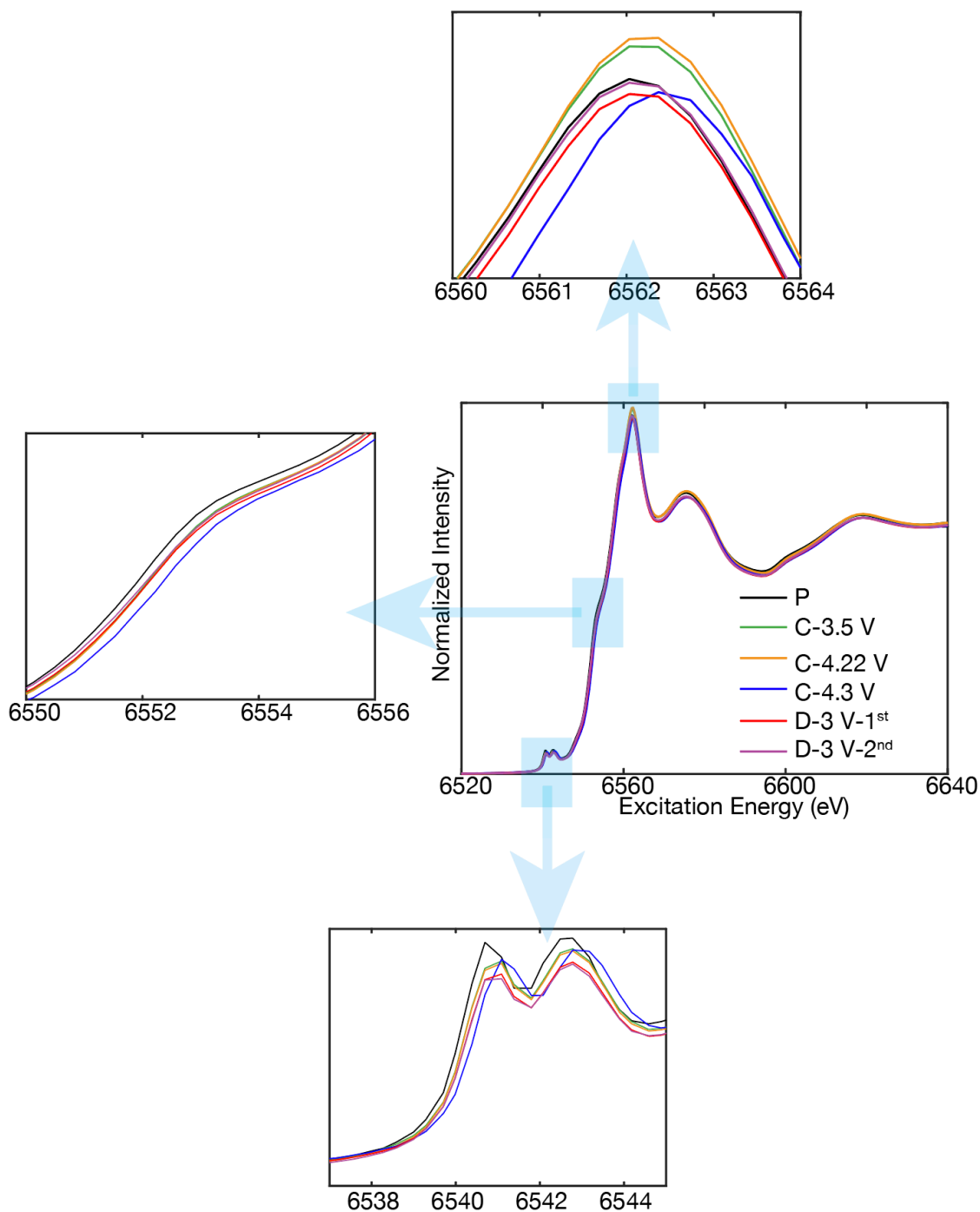
Fig. S5. Mn-K edge of Na₂₋ₓMn₃O₇. The magnified region of the absorption edge (left), white line (top) and pre-edge (bottom) of the Mn K-edge XANES (right). Upon cycling, the shift in the Mn-Kedge is negligible indicating that bulk Mn redox does not contribute to capacity. The spectral shift is consistent in all-regions (by 0.4 eV) indicating that the change is coming from the normalization process rather than charging induced structural or spectroscopic changes in the

material. In addition, if there were changes in the local structure/coordination we would have observed changes in the shape of the pre-edge, which was not evident.
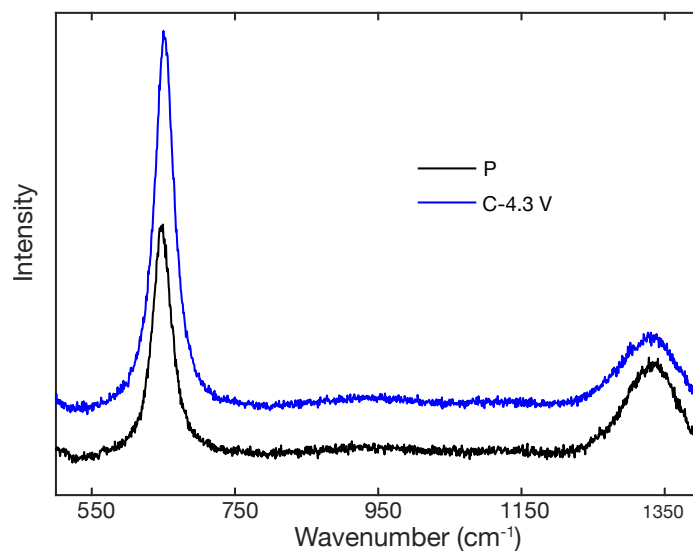

Fig. S6. Raman spectroscopy and absence of O-O dimer formation. A Raman peak at ~800 cm^{-1} has been assigned to the formation of O-O dimer.[17,18] The absence of this peak in $Na_{2-x}Mn_3O_7$ confirms O-O dimer formation does not occur.
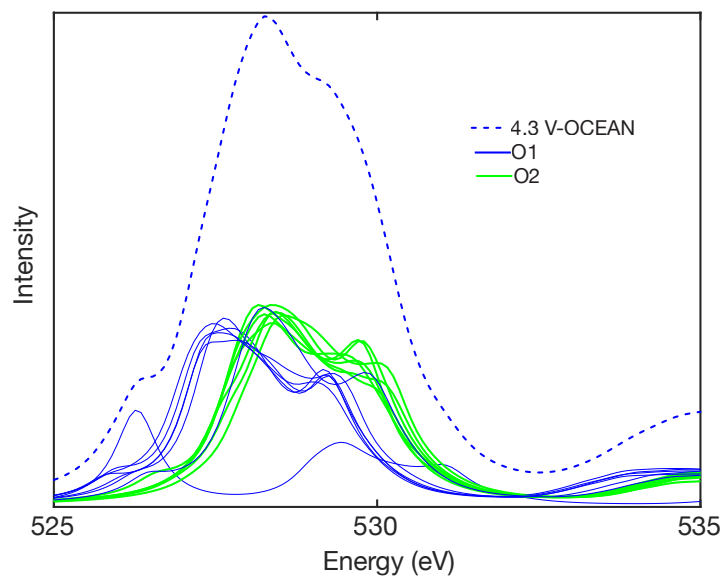
Fig. S7. Simulated O *K*-edge XAS of 25% desodiated material (Na$_{1.5}$Mn$_3$O$_7$). The simulated XAS spectra of both 25% and 50% desodiated samples have the peak at ~527.5 eV (localized hole polarons are formed on both cases).
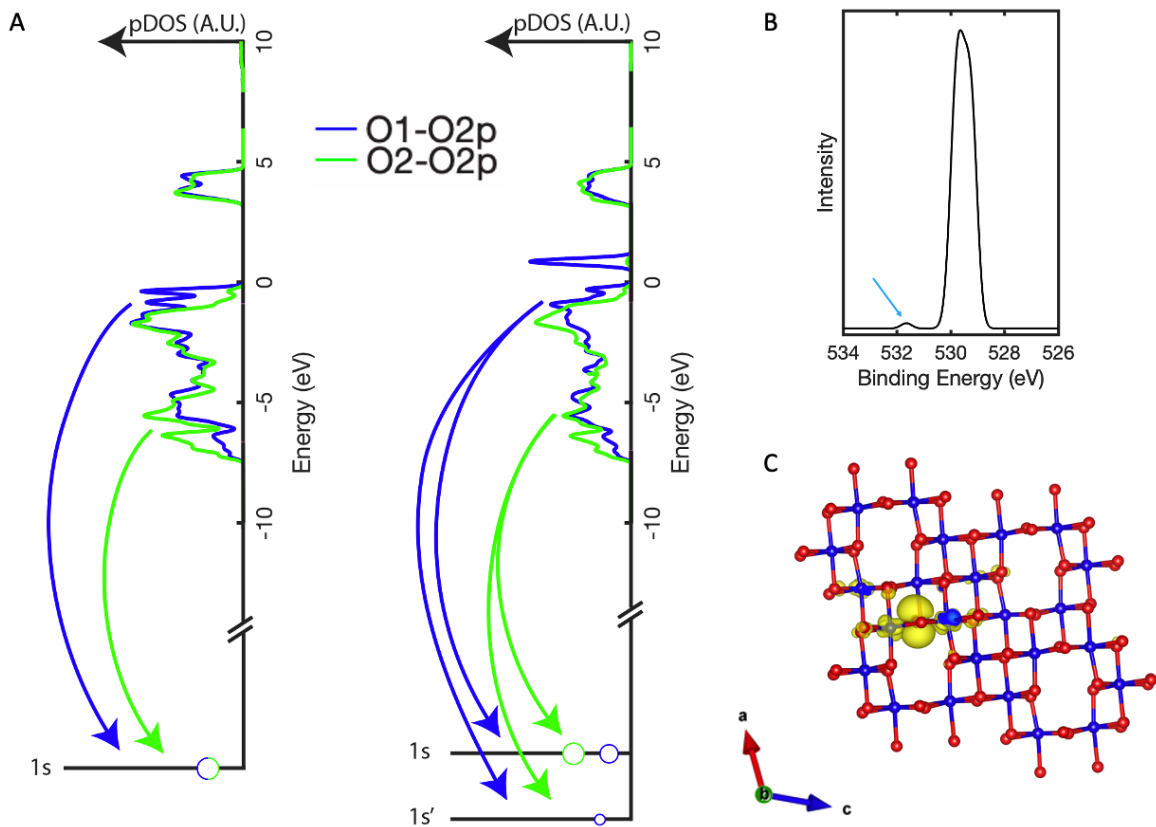
Fig. S8. Estimating the chemical shift of the core hole. (A) Schematic showing the emission process from the valence band. The chemical shift of *1s* electrons on O⁻ ions to lower energies relative to O^{2-} is also indicated schematically. The blue and green arrows indicate decay process from O1 and O2 oxygens, respectively. (**B**) X-ray photoemission spectroscopy (XPS) simulation of charged state of $Na_1Mn_3O_7$. (C) Hole polaron formed in the charged state.
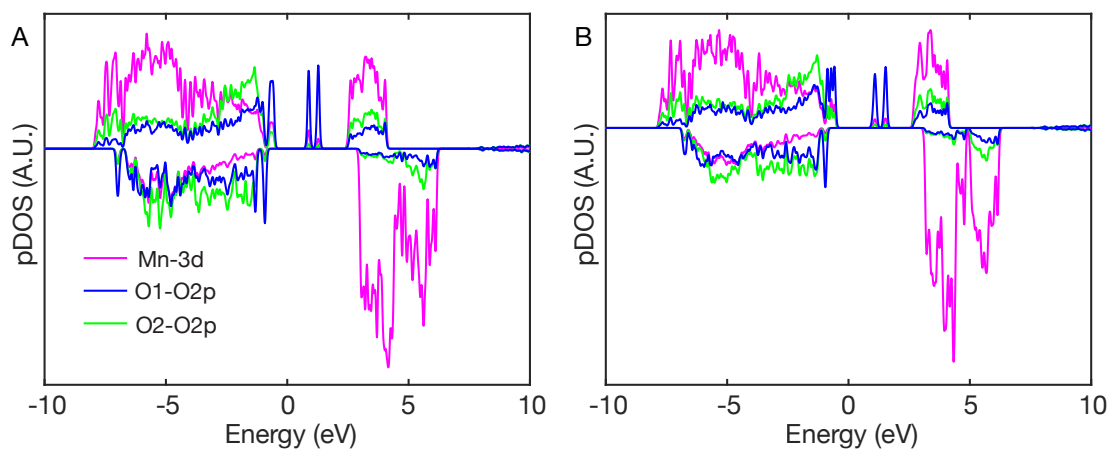
Fig. S9. **Density of States of (A) first (1NN) and (B) second nearest neighbor (2NN) conFig.urations (Na₁Mn₃O₇).** Both configurations (Fig. 4) have a overly similar electronic density of states. The 2NN acceptor state eigenenergy is ~0.2 eV higher in the band gap relative to the valence band maximum suggesting it is slightly more stable than the 1NN configuration.
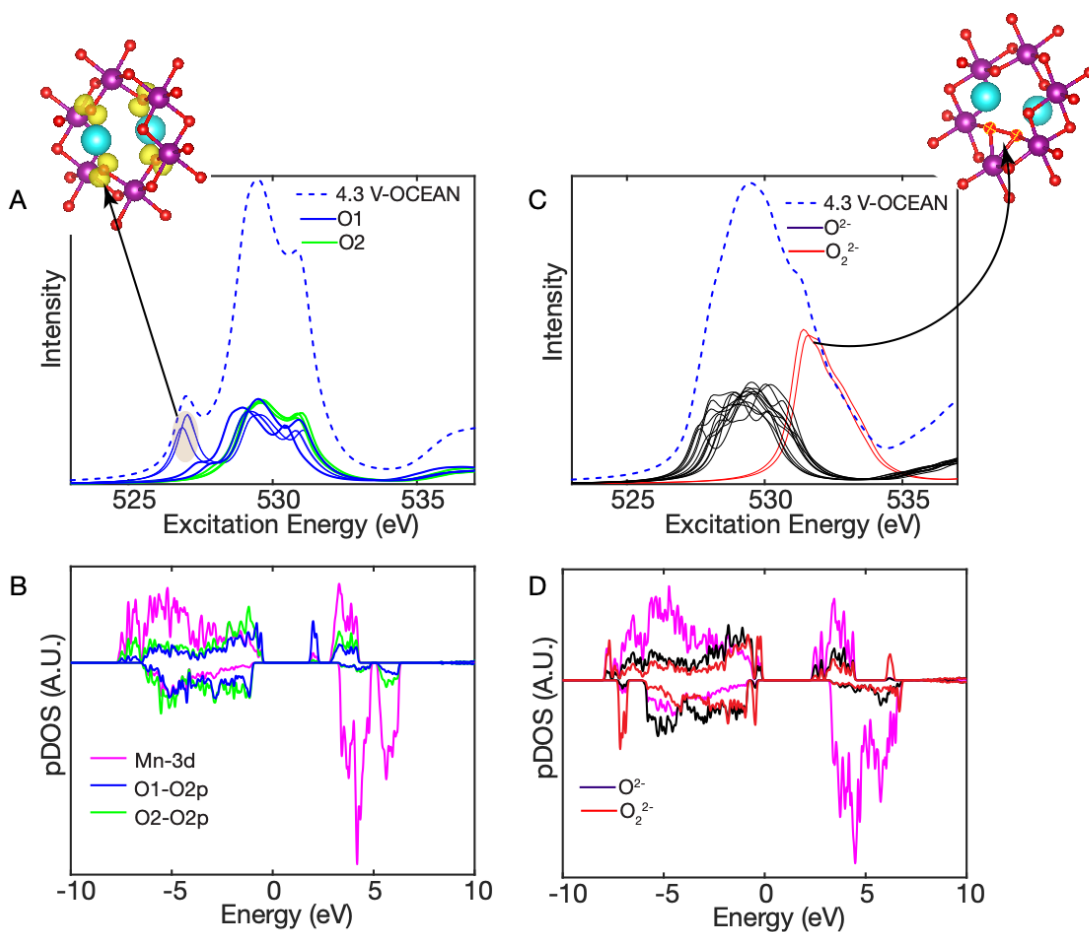
Fig. S10. XAS simulation and density of states of different hole configurations (Na$_1$Mn$_3$O$_7$). XAS simulation (A) and DFT DOS calculations (B) of the split-hole polaron configuration. The four O1 sites holes reside on have overlapping XAS contributions that give rise to the 527.5 eV peak as indicated by the shaded region in (A). XAS simulations for the 3NN (Fig. 4B) and split-hole polaron configurations give similar spectroscopic signatures (peak near 527.5 eV). XAS simulation (C) and DFT DOS calculations (D) of a peroxo bi-polaron with 1.44 Å O-O distance. The peroxo oxygens (marked with yellow crosshair on the desodiated structure) exhibit large spectral weight peaked at 531 eV confirming the experimentally observed[19–21] at 531 eV feature in RIXS and XAS is indeed from the peroxo dimer.

Table S1: Split-hole configuration: We emphasize here that the surprising split-hole configuration (Fig. S11, Fig. 4) is not a result of the incomplete cancellation of the self-interaction error (SIE) or the related delocalization error in approximate DFT.[22] As has long been known, semi-local DFT approximations tend to fully or partially de-localize O^- hole in semi-conducting/insulating oxides due to the delocalization error.[23] The non-local HSE06 functional used in this study is however capable of describing O^- hole localization and concomitant electron-phonon coupling effects that lead to small polaron formation in oxides with band gaps in the few eV range.[23,24] To the extent that the total energy $E(N)$ with respect to fractional particle number N is too convex leading to a delocalization error, increasing the fraction of nonlocal Fock exchange in screened hybrid functionals such as HSE06 towards the unscreened Hartree-Fock (HF) limit provides a means of rendering $E(N)$ less convex. We therefore increased the fraction of Fock exchange in the HSE06 screened hybrid to 35% from the optimal 25% value as a test. We label these functionals HSE-35, HSE-25 respectively. HSE-35 should feature an $E(N)$ that is *less convex* than HSE-25. At the geometries predicted by HSE-25 for 50% desodiaton, we calculated the relative energies of the fully localized 3NN and partly-delocalized split-hole configurations within HSE-25, HSE-35 and a PBE+U approach. The PBE+U calculation employed on-site Hubbard-U parameters $U_d = 3.9$ eV and $U_{2p} = 6.0$ eV. As shown in Table S1, we find relative to the fully localized 3NN configuration, the partially delocalized split-hole configuration is predicted to be *more stable* in HSE-35 than in HSE-25. Therefore, the prediction of the stability of the split-hole in HSE-25 is not because $E(N)$ is too convex or the resulting delocalization error. In contrast, we find that the PBE+U method, which applies on-site corrections to Mn-$3d$ and O-$2p$ orbitals to mitigate the delocalization error on a site by site basis, does not correct for the over-screening of long-range Coulomb interactions in semi-local DFT and predicts the localized 3NN configuration as more stable. This qualitative difference is due to the over-screening of the attractive Coulomb interaction between the O1 holes and the octahedral Na vacancy sites in PBE+U. Thus $Na_{2-x}Mn_3O_7$ presents an interesting illustration of the competition between on-site O-$2p$ exchange interactions that favor full localization and non-local Coulomb interactions that favor a split-hole configuration.

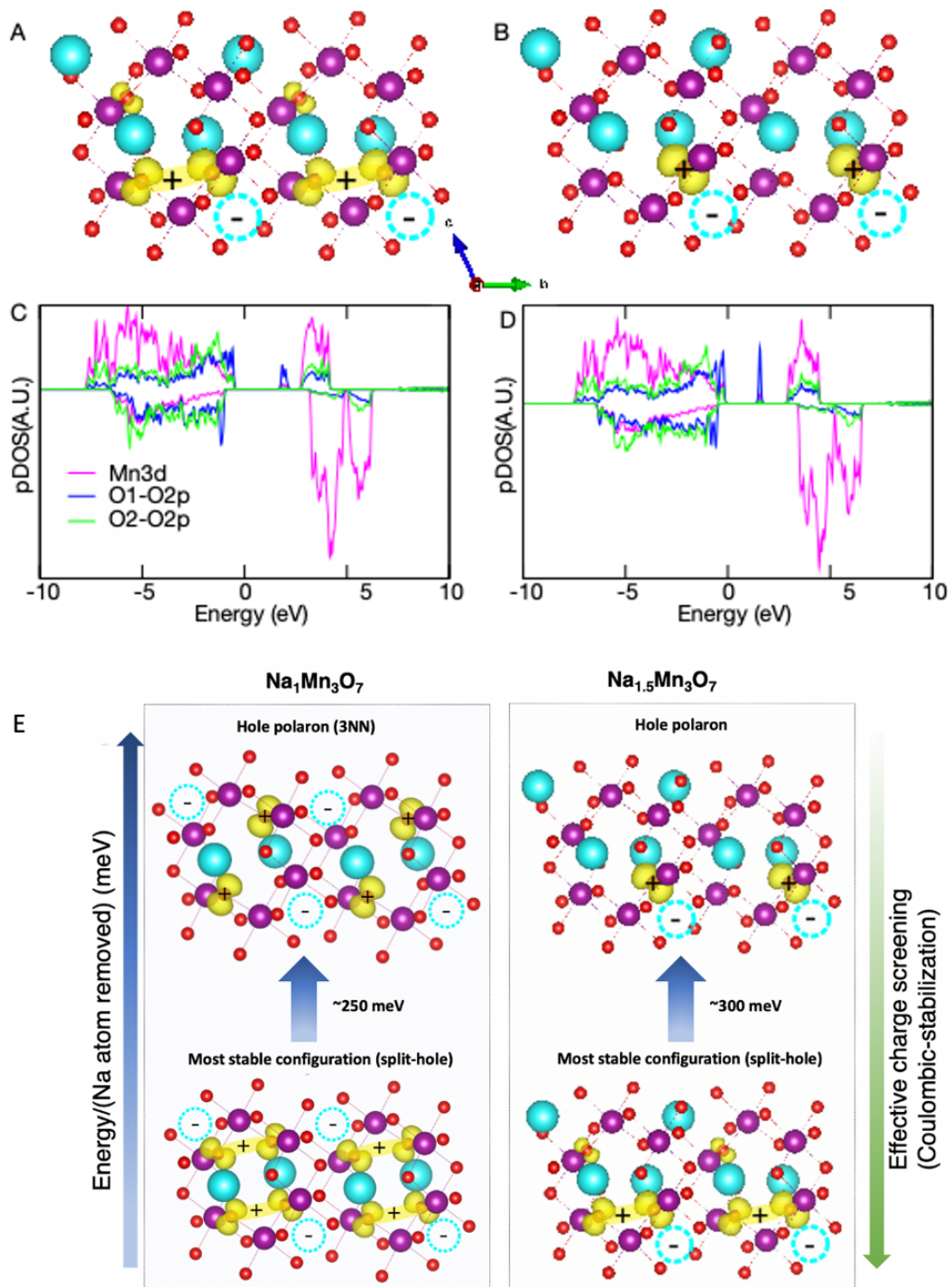| DFT XC approximation	Energy of 3NN relative to split-hole (eV/hole)
HSE-25	0.23
HSE-35	0.33
PBE+U	-0.11

Fig. S11. Coulombic stabilization at different depth of desodiation. (A) & (B)Structure and density of states after 25% charging ($Na_{1.5}Mn_3O_7$). (A) The split-hole polaron is predicted as a stable configuration for an ordered Na2 vacancy (octahedral sodium vacancy) arrangement at 25%

desodiation (more stable than the localized hole (B) by 0.3 eV). At this low level of desodiation, depending on the Na cation ordering near the vacancy site we expect to see a mixture of the split-hole and the localized polaron configurations. (C) and (D) density of states of structures in (A) and (B), respectively. The acceptor states in the split-hole configuration (C) lie higher in the band gap (closer to the conduction band minimum) than in the localized hole configuration (D). (E) The split-hole polaron is the most stable configuration obtained from HSE calculations at both 25% and 50% of desodiation (Fig. 4) since the configuration enhances charge screening (coulombic stabilization).
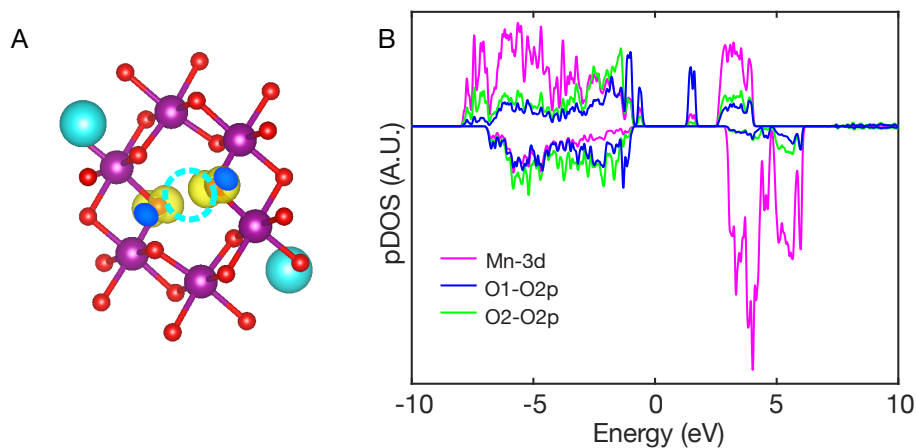

Fig. S12. Structure and density of states after removing Na ions in prismatic sites (Na1) up on charging (Na₁Mn₃O₇). The 3NN configuration is the most stable configuration (A) and its density of state is shown in (B).
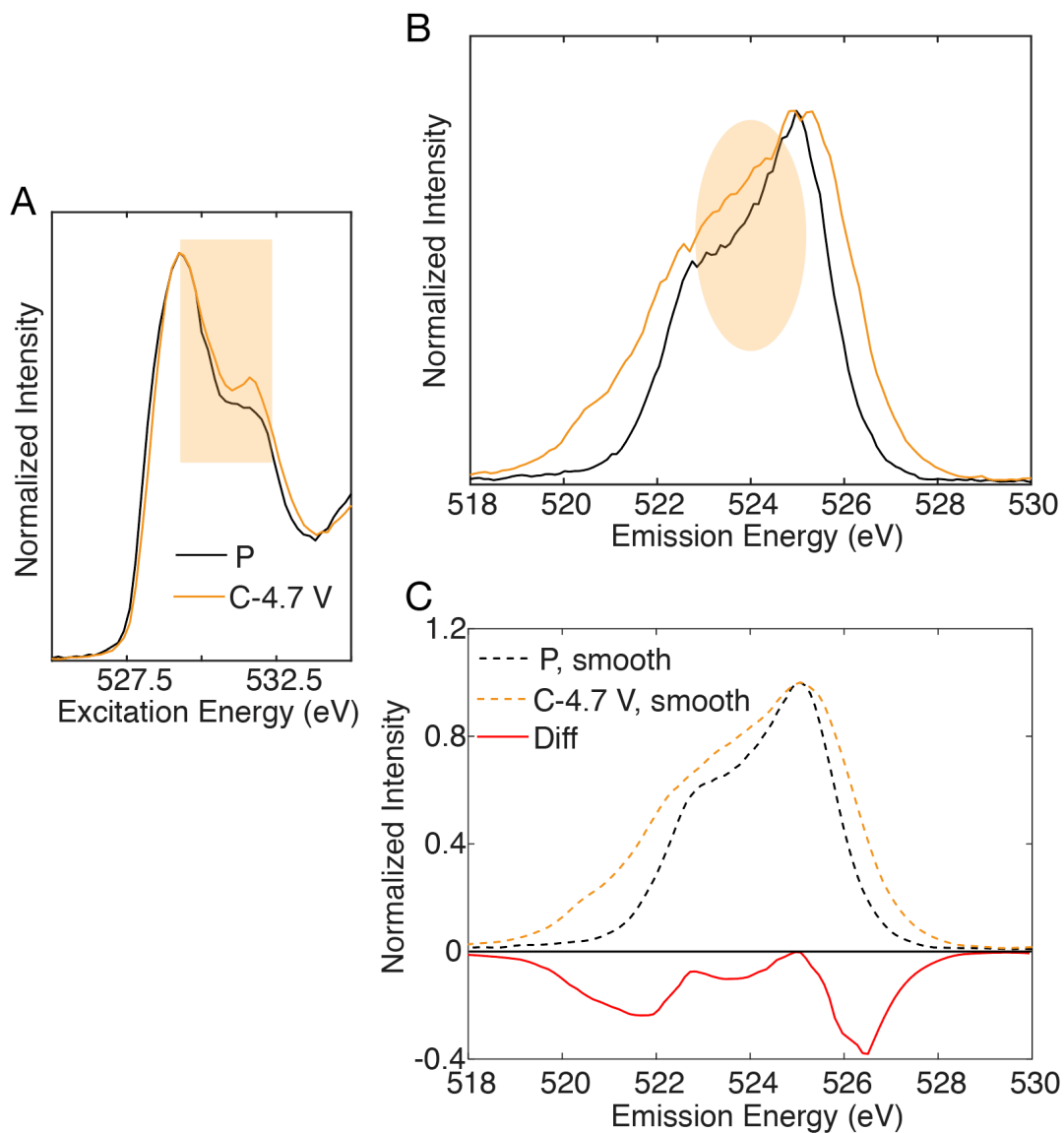
Fig. S13. O-O dimer formation after 2 days of electrode harvesting. (A) The XAS hole polaron feature disappears after 2 days of electrode harvesting and a new peak emerges ~531 eV (shaded region). (B) RIXS spectra ~531 eV excitation energy. A new peak ~523 eV emission energy. (C) Difference of smoothed emission spectra in (B) showing clear difference between charged and pristine state. These features in XAS and RIXS indicate formation of O-O dimer 2 days after electrode harvesting.

Assessing the strength of the π-type interactions between O 2p and Mn t$_{2g}$

We have carried out additional simulations to assess the magnitude of π-type interactions between O 2p and Mn t$_{2g}$ orbitals, Fig. S14. We find that oxygen 2p orbitals have no significant crystal orbital overlap population (COOP) with Mn t$_{2g}$ orbitals (red arrow) that could be correlated with hole formation upon charging. In addition, integration or COOP up to the Fermi level is proportional to the bond order, and we found that the integrated COOP (for both spin-up and -down) increased by less than 5% upon charging. The related antibonding peaks correlated to hole formation (labeled "1" in (Fig. S14D)) are ~20x smaller than the main antibonding Mn t$_{2g}$ and O 2p overlap (labeled "2" in (Fig. S14D)). This indicates the localized nature of the oxygen 2p orbitals and the π -interaction is too weak a factor to be the major stabilization mechanism for hole formation (that is, compared to coulombic stabilization and a kinetic barrier for O-O dimer formation). If O$^-$ was stabilized by π-type interactions, the Mn–O bonds would show more of a bonding characteristic with a considerable COOP between the oxygen 2p and Mn t$_{2g}$ orbitals.
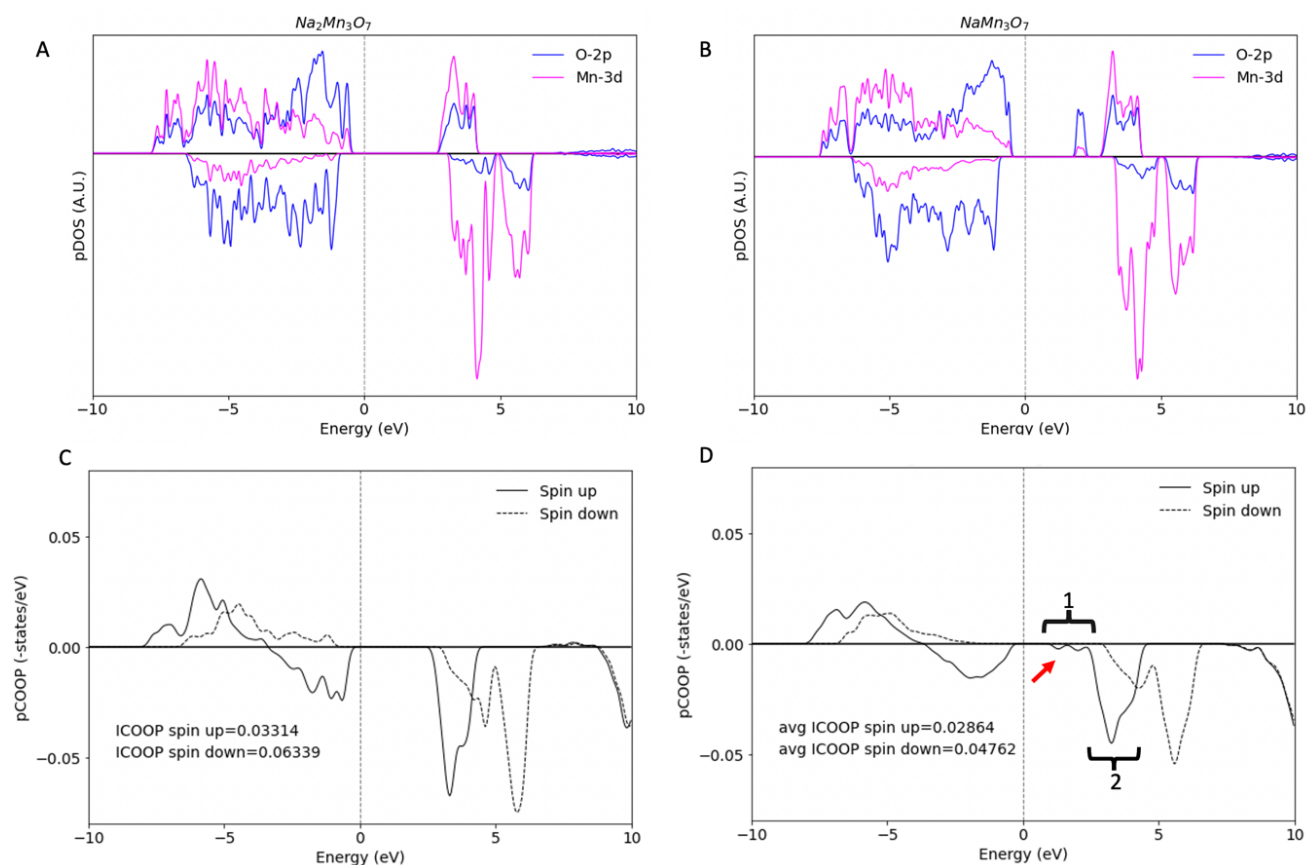

Fig. S14. Density of state (DOS) and crystal orbital overlap population (COOP) of the Mn-O bond. DOS of pristine ($Na_2Mn_3O_7$) (A) and charged ($NaMn_3O_7$ with split-hole configuration) (B) state. COOP of Mn-O bond in pristine (C) and charged (D) state. "1" and "2" in (D) refers to the two antibonding peaks. No significant COOP is observed between oxygen 2p orbitals Mn t$_{2g}$ orbitals (red arrow) that is correlated to hole state formation upon charging.

Reference (Supplementary Reference, RS)

1. Qiao, R. *et al.* High-efficiency in situ resonant inelastic x-ray scattering (iRIXS) endstation at the Advanced Light Source. *Rev. Sci. Instrum.* **88**, 033106 (2017).

2. Ravel, B. & Newville, M. ATHENA,ARTEMIS,HEPHAESTUS: data analysis for X-ray absorption spectroscopy usingIFEFFIT. *J. Synchrotron Radiat.* **12**, 537–541 (2005).

3. Kresse, G. & Furthmüller, J. Efficient iterative schemes for ab-initio total-energy calculations using a plane-wave basis set. *Phys. Rev. B* **54**, 11169–11186 (1996).

4. Kresse, G. & Joubert, D. From ultrasoft pseudopotentials to the projector augmented-wave method. *Phys. Rev. B* **59**, 1758–1775 (1999).

5. Heyd, J., Scuseria, G. E. & Ernzerhof, M. Hybrid functionals based on a screened Coulomb potential. *J. Chem. Phys.* **124**, 219906 (2006).

6. Chang, F. M. & Jansen, M. Darstellung und Kristallstruktur von $Na_2Mn_3O_7$. *Z. Anorg. Allg. Chem.* **531**, 177–182 (1985).

7. Dudarev, S. L., Botton, G. A., Savrasov, S. Y., Humphreys, C. J. & Sutton, A. P. Electron-energy-loss spectra and the structural stability of nickel oxide: An LSDA U study. *Phys. Rev. B* **57**, 1505–1509 (1998).

8. Perdew, J. P., Burke, K. & Ernzerhof, M. Generalized Gradient Approximation Made Simple. *Phys. Rev. Lett.* **77**, 3865–3868 (1996).

9. Jain, A. *et al.* Formation enthalpies by mixing GGA and GGA+*U* calculations. *Phys. Rev. B* **84**, 045115 (2011).

10. Wang, Z., Brock, C., Matt, A. & Bevan, K. H. Implications of the DFT U method on polaron properties in energy materials. *Phys. Rev. B* **96**, 125150 (2017).

11. Vinson, J., Rehr, J. J., Kas, J. J. & Shirley, E. L. Bethe-Salpeter equation calculations of core excitation spectra. *Phys. Rev. B* **83**, 115106 (2011).

12. Gilmore, K. *et al.* Efficient implementation of core-excitation Bethe–Salpeter equation calculations. *Comput. Phys. Commun.* **197**, 109–117 (2015).

13. Giannozzi, P. *et al.* QUANTUM ESPRESSO: a modular and open-source software project for quantum simulations of materials. *J. Phys. Condens. Matter* **21**, 395502 (2009).

14. Shirley, E. L. Theory and simulation of resonant inelastic X-ray scattering in s–p bonded systems: graphite, hexagonal boron nitride, diamond, and cubic boron nitride. *J. Electron Spectrosc.* **110–111**, 305–321 (2000).

15. Vinson, J., Jach, T., Müller, M., Unterumsberger, R. & Beckhoff, B. Quasiparticle lifetime broadening in resonant x-ray scattering ofNH_4NO_3. *Phys. Rev. B* **94**, 035163 (2016).

16. Heyd, J., Scuseria, G. E. & Ernzerhof, M. Hybrid functionals based on a screened Coulomb potential. *J. Chem. Phys.* **118**, 8207–8215 (2003).

17. Qiao, Y. *et al.* Reversible anionic redox activity in Na_3RuO_4 cathodes: a prototype Na-rich layered oxide. *Energy Environ. Sci.* **11**, 299–305 (2018).

18. Li, X. *et al.* Direct Visualization of the Reversible O^{2-}/O^{-} Redox Process in Li-Rich Cathode Materials. *Adv. Mater.* **30**, 1705197 (2018).

19. Gent, W. E. *et al.* Coupling between oxygen redox and cation migration explains unusual electrochemistry in lithium-rich layered oxides. *Nat. Commun.* **8**, 2091 (2017).

20. Hong, J. *et al.* Metal–oxygen decoordination stabilizes anion redox in Li-rich oxides. *Nat. Mater.* **18**, 256–265 (2019).

21. Gent, W. E., Abate, I. I., Yang, W., Nazar, L. F. & Chueh, W. C. Design rules for high-Valent redox in intercalation electrodes. *Joule* **4**, 1369–1397 (2020).

22. Mori-Sánchez, P., Cohen, A. J. & Yang, W. Localization and delocalization errors in density functional theory and implications for band-gap prediction. *Phys. Rev. Lett.* **100**, 146401 (2008).

23. Lany, S. Predicting polaronic defect states by means of generalized Koopmans density functional calculations. *Phys. Status Solidi* **248**, 1052–1060 (2011).

24. Droghetti, A., Pemmaraju, C. D. & Sanvito, S. Polaronic distortion and vacancy-induced magnetism in MgO. *Phys. Rev. B* **81**, 092403 (2010).